



# The Host Galaxy of the Recoiling Black Hole Candidate in 3C 186: An Old Major Merger Remnant at the Center of a $z = 1$ Cluster

T. Morishita<sup>1,2</sup>, M. Chiaberge<sup>3,4</sup>, B. Hilbert<sup>1</sup>, E. Lambrides<sup>4</sup>, L. Blecha<sup>5</sup>, S. Baum<sup>6</sup>, S. Bianchi<sup>7</sup>, A. Capetti<sup>8</sup>, G. Castignani<sup>9,10</sup>, F. D. Macchetto<sup>1</sup>, G. K. Miley<sup>11</sup>, C. P. O’Dea<sup>6</sup>, and C. A. Norman<sup>1,4</sup>

<sup>1</sup> Space Telescope Science Institute, 3700 San Martin Drive, Baltimore, MD 21218, USA

<sup>2</sup> IPAC, California Institute of Technology, MC 314-6, 1200 E. California Boulevard, Pasadena, CA 91125, USA

<sup>3</sup> Space Telescope Science Institute for the European Space Agency (ESA), ESA Office, 3700 San Martin Drive, Baltimore, MD 21218, USA

<sup>4</sup> The William H. Miller III Department of Physics and Astronomy, Johns Hopkins University, Baltimore, MD 21218, USA

<sup>5</sup> University of Florida, Department of Physics, 2001 Museum Rd., Gainesville, FL 32611, USA

<sup>6</sup> Department of Physics and Astronomy, University of Manitoba, Manitoba, Canada

<sup>7</sup> Dipartimento di Matematica e Fisica, Università degli Studi Roma Tre, via della Vasca Navale 84, I-00146 Roma, Italy

<sup>8</sup> INAF—Osservatorio Astrofisico di Torino, Pino Torinese, Italy

<sup>9</sup> Dipartimento di Fisica e Astronomia “Augusto Righi”, Alma Mater Studiorum Università di Bologna, Via Gobetti 93/2, I-40129 Bologna, Italy

<sup>10</sup> INAF—Osservatorio di Astrofisica e Scienza dello Spazio di Bologna, via Gobetti 93/3, I-40129, Bologna, Italy

<sup>11</sup> Leiden Observatory, University of Leiden, P.O. Box 9513, 2300 RA Leiden, The Netherlands

Received 2021 December 13; revised 2022 April 20; accepted 2022 April 23; published 2022 June 7

## Abstract

3C 186, a radio-loud quasar at  $z = 1.0685$ , was previously reported to have both velocity and spatial offsets from its host galaxy, and has been considered as a promising candidate for a gravitational wave recoiling black hole triggered by a black hole merger. Another possible scenario is that 3C 186 is in an ongoing galaxy merger, exhibiting a temporary displacement. In this study, we present analyses of new deep images from the Hubble Space Telescope WFC3-IR and Advanced Camera for Surveys, aiming to characterize the host galaxy and test this alternative scenario. We carefully measure the light-weighted center of the host and reveal a significant spatial offset from the quasar core ( $11.1 \pm 0.1$  kpc). The direction of the confirmed offset aligns almost perpendicularly to the radio jet. We do not find evidence of a recent merger, such as a young starburst in disturbed outskirts, but only marginal light concentration in F160W at  $\sim 30$  kpc. The host consists of mature ( $\gtrsim 200$  Myr) stellar populations and one compact star-forming region. We compare with hydrodynamical simulations and find that those observed features are consistently seen in late-stage merger remnants. Taken together, those pieces of evidence indicate that the system is not an ongoing/young merger remnant, suggesting that the recoiling black hole scenario is still a plausible explanation for the puzzling nature of 3C 186.

*Unified Astronomy Thesaurus concepts:* Active galaxies (17); Gravitational waves (678)

## 1. Introduction

In the current paradigm of  $\Lambda$ -CDM cosmology, galaxy–galaxy mergers play many important roles in galaxy evolution (Volonteri et al. 2003; Springel 2005). Supermassive black hole (SMBH) merger is one such role expected as a result of major galaxy mergers. To explain tight relationships such as the  $M$ – $\sigma$  relation (Ferrarese & Merritt 2000; Gebhardt et al. 2000), an intimate relationship between galaxy growth and black hole growth during mergers seems to be required (e.g., Peng 2007).

Black hole mergers are thought to happen in three phases: the two black holes are pulled toward the center of the gravitational potential of the merged galaxy by dynamical friction; they become a binary system by losing angular momentum via gravitational slingshot interaction with stars that have appropriate angular momentum in the region of the parameter space (the so-called loss cone; Frank & Rees 1976; Begelman et al. 1980) and gas-driven inspiral (e.g., Escala et al. 2005; Dotti et al. 2007); in the final phase, the bound pair may lose the remaining angular momentum via the emission of gravitational waves (GWs), and eventually the two black holes coalesce. In most cases, these GWs are emitted anisotropically.

Depending on both the relative orientation of the spins of the merging black holes and their mass ratio, the merged black hole may receive a recoil kick (Centrella et al. 2010; Blecha et al. 2011; Komossa 2012) with a velocity as high as  $\sim 5000$  km s<sup>−1</sup> (e.g., Campanelli et al. 2007; Tichy & Marronetti 2007; Lousto & Zlochower 2011). As a result, the merged black hole may show displacement from the center of the host galaxy in both position and velocity.

However, the details of the mechanisms that bring the two black holes to the distance at which GW emission becomes substantial are still poorly understood. This is called the final-parsec problem (e.g., Milosavljević & Merritt 2003). For example, if the loss cone is not replenished quickly enough for the SMBH pair to get sufficiently close and lose energy via GWs, the pair may stall and never merge; such situations may be observed as dual quasars or pairs of less active AGNs (active galactic nuclei) (e.g., Komossa et al. 2003; Hennawi et al. 2006; Goulding et al. 2019; Silverman et al. 2020; O’Neill et al. 2022). If this is often the case and prevents SMBH pairs from merging, our current understanding of the mechanisms for black hole growth may need significant revisions. It is thus important to find evidence, either direct (GWs) or indirect (recoiling black holes), of SMBH mergers. While we still need to wait for the next generation of space-based GW interferometers and pulsar timing arrays for direct confirmation in the black hole mass range of  $M_{\text{BH}} \gtrsim 10^8 M_{\odot}$ .



Original content from this work may be used under the terms of the [Creative Commons Attribution 4.0 licence](https://creativecommons.org/licenses/by/4.0/). Any further distribution of this work must maintain attribution to the author(s) and the title of the work, journal citation and DOI.

(see, e.g., Moore et al. 2015), identifying recoiling black holes helps us to advance our understanding of such extreme events.

Today, there are several candidates for recoiling black holes, with velocity offsets (Komossa et al. 2008; Steinhardt et al. 2012; Comerford & Greene 2014; Pesce et al. 2018), spatial offsets (Batcheldor et al. 2010; Koss et al. 2014; Lena et al. 2014; Barrows et al. 2016; Skipper & Browne 2018), or both (Hogg et al. 2021; Pesce et al. 2021). In particular, high-velocity offsets ( $>1000 \text{ km s}^{-1}$ ) are expected to be rare, but they are more likely to be observed in combination with large spatial offsets (e.g., Blecha et al. 2016) and thus can be used as a proxy for ideal follow-up targets.

For example, CID-42, a radio-quiet AGN at  $z = 0.36$ , shows a velocity offset between the narrow and broad components of the  $\text{H}\beta$  emission line of  $\sim 1300 \text{ km s}^{-1}$ , with two nuclei in Hubble Space Telescope (HST) images displaced by  $\sim 2.5 \text{ kpc}$  in projected distance (Civano et al. 2010, 2012; Blecha et al. 2013; Novak et al. 2015). The presence of a second, obscured radio-quiet AGN, however, cannot be excluded (but see also Kim et al. 2017). Another intriguing case is found in A2261-BCG, the brightest cluster galaxy (BCG) in A2261 at  $z = 0.2248$ . This galaxy was found to have an unusually flat core profile, with an offset of  $\sim 0.7 \text{ kpc}$  from the photocenter of the surrounding envelope (Postman et al. 2012). The follow-up study presented spectroscopic measurements of three of the four knots identified in the central region, to test the hypothesis that the massive black hole was ejected from the core and harbors within one of those knots (Burke-Spolaor et al. 2017). Their observations could not identify the precise location of the expected SMBH ( $\sim 10^{10} M_{\odot}$ ), leaving the conclusion still pending.

3C 186 is another promising candidate, but at far higher redshift than others. The system is a radio-loud quasar ( $\sim 10^5 \text{ yr}$ ; Murgia et al. 1999; Siemiginowska et al. 2005) of the compact-steep spectrum class (Fanti et al. 1985; O’Dea 1998; O’Dea & Saikia 2021), located in the center of a cluster of galaxies at  $z = 1.0685$ , with an SMBH of  $\sim (3\text{--}6) \times 10^9 M_{\odot}$  (Kuraszkiewicz et al. 2002; Chiaberge et al. 2017).

3C 186 was recently observed as one of 22 3C radio galaxies/quasars in a snapshot program of HST (Hilbert et al. 2016). Chiaberge et al. (2017) reported its spatial offset to be  $1''.3 \pm 0''.1$ , or  $\sim 11 \text{ kpc}$ , with respect to the center of the host galaxy seen in their medium-deep image of WFC3-IR F140W. In the same study, 3C 186 was also revealed to have a significant velocity offset ( $\sim 2140 \text{ km s}^{-1}$ ) of broad lines associated with the quasar with respect to the systemic redshift of the host measured by two narrow lines, [O II] and [Ne III], suggestive of a binary black hole merger with a mass ratio  $m_1/m_2 > 0.25$  (Lousto et al. 2017). In addition, the follow-up observations with Keck/OSIRIS integral field unit (IFU) revealed a tentative but significant velocity shift ( $>1800 \text{ km s}^{-1}$ ) in the broad component of the  $\text{H}\beta$  line from narrow lines (Chiaberge et al. 2018, see also Section 4.4).

While all previous results support the interpretation of 3C 186 as a GW recoiling black hole, there are two other possible scenarios that may explain the observed properties: one is that we are seeing an ongoing galaxy merger, where its photocenter is temporarily displaced due to disturbances in the host morphology; the other scenario is that the quasar is associated with an undermassive galaxy that is superimposed on another brighter galaxy.

**Table 1**  
Summary of HST Observations in the 3C 186 Field

Instrument	Filter	Total Exposure Time (s)
ACS-WFC	F606W	5567
WFC3-IR	F110W	5042
WFC3-IR	F160W	7563

With the depth of the previous F140W image, those scenarios were not completely excluded, as tidal features and recent star formation in the outskirts can easily be missed (e.g., Koss et al. 2018). Deeper imaging with HST is thus important to unveil any evidence of ongoing merger and constrain the current stage of the system.

The aim of this paper is to test these alternative hypotheses by analyzing deeper IR and optical images newly taken in the HST Cycle 25. In particular, high photometric sensitivity of HST at  $\sim 1 \text{ kpc}$  resolution provides details of the underlying stellar population of the host galaxy and allows us to further constrain the timescale since the last major merger and associated star formation.

Throughout, we adopt the AB magnitude system (Oke & Gunn 1983; Fukugita et al. 1996), cosmological parameters of  $\Omega_m = 0.3$ ,  $\Omega_{\Lambda} = 0.7$ ,  $H_0 = 70 \text{ km s}^{-1} \text{ Mpc}^{-1}$ , and the Salpeter (1955) initial mass function. We refer to magnitude for the HST filters used in this study, F606W, F110W, and F160W as  $V_{606}$ ,  $J_{110}$ , and  $H_{160}$ , respectively.

## 2. Data

### 2.1. HST Observations and Data Reduction

3C 186 was observed in a General Observer program (PID 15254; PI. M. Chiaberge) during the HST Cycle 25 with WFC3-IR and Advanced Camera for Surveys (ACS). Two filters, F110W and F160W, are used in the WFC3 observations and one filter, F606W, in the ACS observations (Table 1). The observing position angle was carefully designed during the phase II process so as to minimize possible contamination of the host galaxy by stellar spikes from the quasar and surrounding objects. To avoid saturation of a few pixels in the quasar core, we started with one short exposure ( $\sim 30 \text{ s}$ ) in each of the five ACS observations (one per orbit). Then, the following exposures were taken at the same location and rotation angle of the first dither point in each orbit, to ensure an identical point-spread function (PSF) profile over all exposures.

To reduce imaging data, we follow the procedure presented in Hilbert et al. (2016). For ACS data, we begin with files in the `flt` format. These images are corrected for charge transfer efficiency (CTE) effects through the CTE correction algorithm (Anderson & Bedin 2010). For WFC3-IR data, we begin with files in the `flt` format, because the multiple nondestructive detector readouts within each observation allowed for easy cosmic-ray identification and removal within the `calwf3` data reduction pipeline. However, pixels subjected to high flux levels in preceding observations are affected by persistence and need to be corrected. To remove any persistence signal present in our data, we begin by retrieving the persistence masks and persistence-corrected `flt` files of our observations from MAST. These files have had the persistence signal modeled and subtracted from them following the model described in Section 8.3 of version 4.0 of the WFC3 Data Handbook, and are

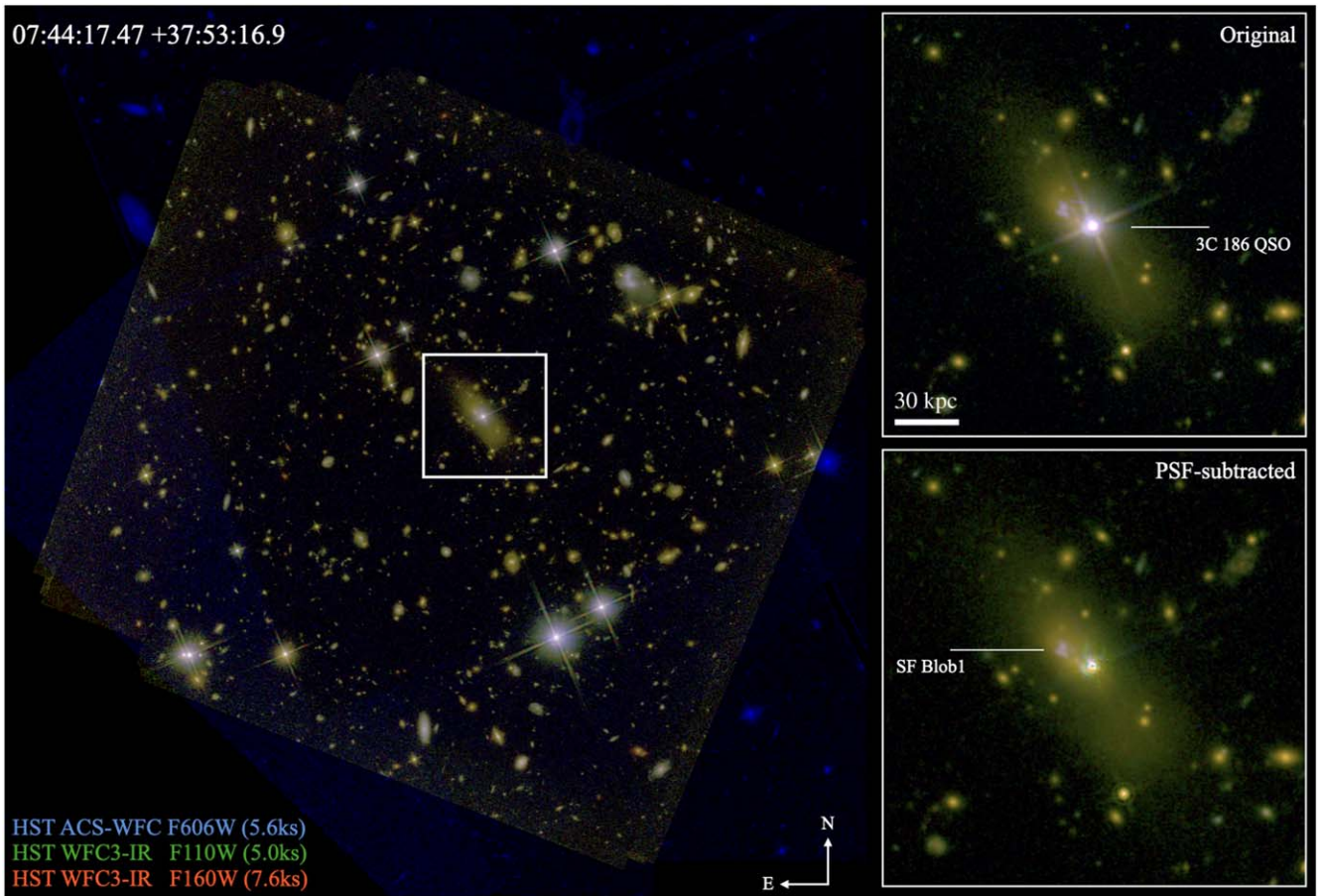


**Figure 1.** Pseudo-color image of the 3C 186 field (F606W for blue, F110W green, F160W red). A zoomed image of 3C 186 ( $\sim 27 \times 27$  arcsec<sup>2</sup>) is shown in the two right panels, in the original (top) and PSF-subtracted (bottom) images. The compact star-forming blob SF Blob1 (Section 3.3) is indicated in the bottom right panel. The images have been rotated so that north is up and east to the left.

therefore different from the standard fit files available in the archive. Before proceeding with the data reduction, we also manually mask the satellite trail present in one of our images.

Since our focus in this study is the host galaxy of 3C 186, we attempt to subtract the light from the bright quasar nucleus in each distortion-uncorrected image (those in *flt/flc* formats) before the geometric correction and final stacking steps (see Section 2.2).

The next step in our data reduction is to remove the geometric distortion from all of the PSF-subtracted *flc/flt* files and to combine images into a final image for each filter. We use *Astrodrizzle* to accomplish both of these steps.

For each filter, we combine the PSF-subtracted images into a final image with a pixel scale of  $0''.045 \text{ pixel}^{-1}$ . We find a value of “5.5 5.0” for the *driz\_cr\_snr* parameter results in good cosmic-ray rejection during the stacking process. We also calculate an optimal *final\_pixfrac* value of 0.75 for our data and final pixel scale.

We then use *Tweakreg* (also part of the *Drizzlepac* software package) to align this final image to the same world coordinate system present in the corresponding ACS drizzled image. At this point, it is possible to overlay the ACS and WFC3 images for a particular object and compare the morphology and brightness in the two observation bands.

The resulting final image is shown in Figure 1. The PSF-subtracted image reveals a clear spatial offset between the

quasar and the host galaxy (Section 3.1). Our deep images also reveal faint outskirts of the host, out to  $\sim 60$  kpc.

## 2.2. PSF Subtraction

In order to subtract the PSF component without over-subtracting the host light component, we fit the observed light profile with PSF+single Sérsic profile using *GALFIT* (Peng et al. 2002). In an effort to achieve the best model fits, we experiment with the *GALFIT* inputs. We create a custom bad pixel file for each exposure, where we remove all nearby astrophysical sources as well as bad pixels and cosmic rays. By supplying this file to *GALFIT*, we reduce the chances that the final fit is contaminated by nearby sources.

The PSFs used for our PSF subtractions are created using *TinyTim* software (Krist et al. 2011). We use *TinyTim* PSFs due to a lack of unsaturated, isolated PSFs with high signal-to-noise ratio (S/N) in our data to use as models. In order to create realistic PSFs, we used characteristics from our observations when creating the model PSFs. We begin by finding the mean secondary mirror focus offset for the date and time of our observation. This information is collected from the HST focus model website.<sup>12</sup>

Other information used as input to *TinyTim* includes the HST instrument and filter, the target’s pixel location on the

<sup>12</sup> <http://www.stsci.edu/hst/observatory/focus/FocusModel>



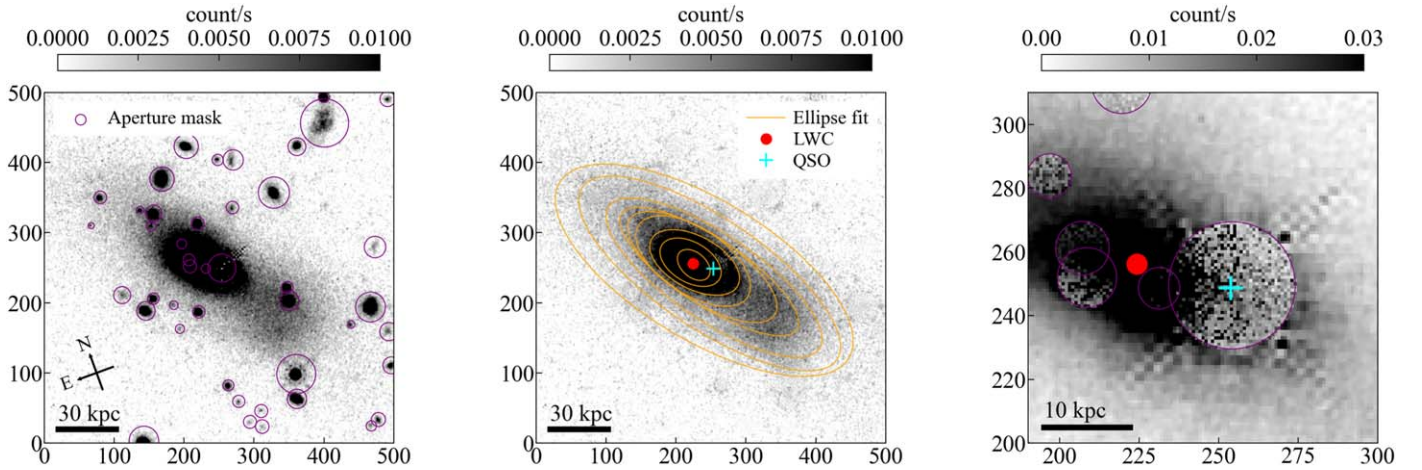


**Figure 2.** Left: PSF-subtracted image of 3C 186 in F160W, in a  $500 \times 500$  pixel postage stamp. Regions that are masked and patched are indicated with purple apertures. Middle: one of the patched images, where all masked regions are filled by random values taken from nearby pixels (Section 3.1). The median light-weighted center (red point), calculated over 100 such realizations, is clearly off from the flux peak position of the quasar (cyan cross). Fitted ellipses are shown (orange lines). Light concentration is seen in the southwest direction from the quasar. Right: enlarged image of the middle panel with different color stretch.

detector, the amount of jitter (0 for this work), and the size in arcseconds of the output model PSF ( $7''$ ). Finally, we also provide a quasar spectrum, in order for TinyTim to determine wavelength-dependent PSF characteristics. For simplicity, we used the composite quasar near-IR spectrum from Glikman et al. (2007) redshifted to  $z \sim 1$ . With this information in hand for each exposure, we run all three stages of TinyTim. The final output is one geometrically distorted model PSF corresponding to each flc/flt image.

We also fit the data using a PSF at the nominal pixel scale, as well as a supersampled PSF. We find that the fit with the supersampled PSF tends to oversubtract the source flux, and therefore keep to the nominal pixel scale for our final fittings. We also fit the data with TinyTim PSFs from a range of focus values, in order to examine any differences. The best modeling and subtraction came from values that match the focus values indicated by the focus model website. Finally, as the data being fit are in units of electrons per second, rather than the electrons that GALFIT assumes, we also experiment with fits where we provide the ERR array of the flt/flc file to GALFIT as a sigma image. We find in this case that the resulting fits again tend to oversubtract the source's flux. With our final set of GALFIT parameters and inputs, we obtain fits with reduced  $\chi^2$  between 0.75 and 1.5. The best-fit PSF component is then subtracted from each of the images before the images are processed for geometric correction and final stacking with Astrodrizzle.

### 3. Analysis and Results

#### 3.1. Light-weighted Center of the Host Galaxy

We estimate the center of mass of the host galaxy by using F160W, which is the deepest among our images here. It is noted that the light distribution in the F160W image is considered to trace the stellar component of the host well, because at the redshift of 3C 186 the filter corresponds to rest-frame  $\sim 0.8 \mu\text{m}$  and is free from strong emission lines (see also Section 3.2).

While the extended light from the host galaxy is clearly visible in the PSF-subtracted image (Figure 1), it is still challenging to accurately estimate its light-weighted center (LWC) due to the fact that fore/background objects are superposed on the host. Especially, since 3C 186 is in a

crowded field, the latter remains as a critical issue because flux contribution from other sources can easily affect the estimate.

To eliminate such flux contamination, we first manually mask regions that are likely to belong to surrounding objects (including the compact star-forming blob discussed in Section 3.3) and residuals at the position of the quasar, by placing circular apertures of arbitrary sizes in the PSF-subtracted F160W image. By doing so, we ensure to mask all possible contaminants, whereas automated software (e.g., SExtractor; Bertin & Arnouts 1996) may not necessarily recognize all objects in crowded regions or might mistakenly mask part of the host. The image with those aperture masks is shown in the left panel of Figure 2. To mask the residuals at the location of the quasar, we place an aperture with radius of  $r = 0''.9$ .

The next step is to fill those masked regions. This process is necessary because leaving those masked pixels could result in a biased estimate of LWC depending on the choice of position and size used of each circular mask. For each pixel of the masked regions, we use a Metropolis–Hastings-like algorithm to randomly select one of the neighboring pixels that are not masked, to fill in the target pixel. This filling process is as follows.

1. For the pixel of interest in a masked region, assign a radius ( $r_{\text{rand}}$ ) randomly taken from the range  $[0, r_{\text{max}}]$ , where we here set  $r_{\text{max}} = 50$  pixels.
2. Compare the probability of  $r_{\text{rand}}$ , assigned by  $p(r) = \exp(-r/r_{\text{max}})$ , with a random float number,  $p_r$ , drawn from the range  $[0, 1]$ .
3. If  $p(r_{\text{rand}}) > p_r$ , then select a random pixel from unmasked regions at  $r_{\text{rand}} < r < r + \Delta r$ , where we set  $\Delta r = 2$  pixels; otherwise return to step 1 and repeat the process until it passes the criterion.
4. Repeat steps 1–3 for all masked pixels.
5. Repeat steps 1–4  $n_{\text{iter}}$  times, to get  $n_{\text{iter}}$  images with the masked regions filled, respectively.

We here set  $n_{\text{iter}} = 100$ . By adopting an exponential function for  $p(r)$ , the filling flux is likely to be chosen from one of the nearby pixels, making the reproduced light profile contiguous, which is reasonable given the primary purpose here. One of the

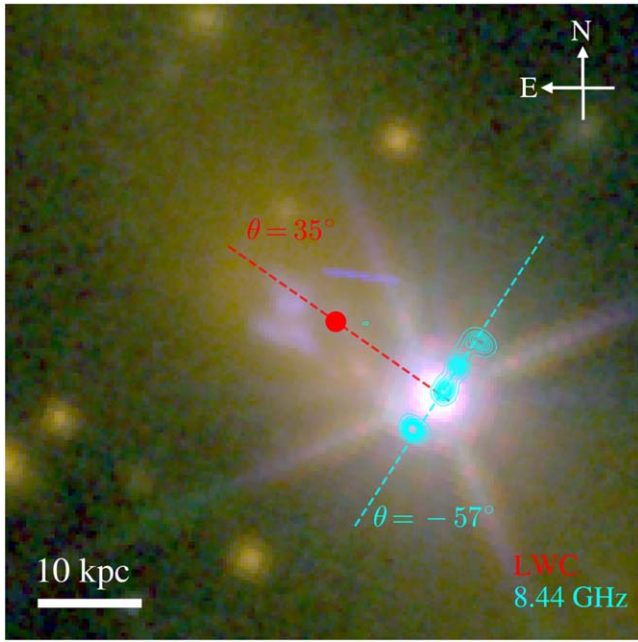


**Figure 3.** Central region of 3C 186. The RGB image is in the same configuration as in Figure 1. The position of the light-weighted center is shown (red circle). The 8.44 GHz radio continuum emission, retrieved from the NRAO Very Large Array archive (project ID AA0129; cyan contour), is overlaid. Two dashed lines are shown to highlight the inferred axes of the offset (red) and the jet (cyan), respectively. The image has been rotated so that north is up and east to the left.

realizations is shown in Figure 2 as an example. While several pixels can occasionally have a value distinct from the average value of surrounding pixels, contributions from such pixels to the determination of LWC are smoothed out after  $n_{\text{iter}}$  realizations.

At each realization of  $n_{\text{iter}}$ , we calculate the LWC from the following equations:

$$\begin{aligned}\bar{x} &= \frac{\sum x f_{160}(x, y) / e_{160}(x, y)^2}{\sum f_{160}(x, y) / e_{160}(x, y)^2}, \\ \bar{y} &= \frac{\sum y f_{160}(x, y) / e_{160}(x, y)^2}{\sum f_{160}(x, y) / e_{160}(x, y)^2}\end{aligned}\quad (1)$$

where  $f_{160}(x, y)$  and  $e_{160}(x, y)$  represent the flux value and its associated rms value at the position  $[x, y]$ , and the sum goes over pixels with  $f_{160}/e_{160} > S/N_{\text{limit}}$  within  $r_{\text{lim}} < 250$  pixels ( $\sim 91$  kpc) from the target. We here set  $S/N_{\text{limit}} = 0.7$ , which is equivalent to the detection threshold (DETECT\_THRESH of SExtractor) used for source detection in the F160W image. We empirically find that the value in general provides reasonable detection out to faint outskirts of sources without being contaminated by background pixels.

We calculate the median LWC over  $n_{\text{iter}}$  realizations and find  $[x, y] = [-29.42^{+0.07}_{-0.08}, 7.44^{+0.06}_{-0.05}]$  (in pixels) with respect to the position of 3C 186 in the image of Figure 2, or 7:44:17.586, +37:53:18.165 in sky coordinates. The 16th/84th percentiles are associated as uncertainties. The result reveals a significant offset of  $1''.37 \pm 0''.01$ , or  $11.1 \pm 0.1$  kpc, in the projected distance, which is consistent with the estimate with a shallower F140W image by Chiaberge et al. (2017). The angle from the LWC toward the quasar core, measured from the west in the clockwise direction, is  $\sim +35^\circ$ , which lies almost perpendicular

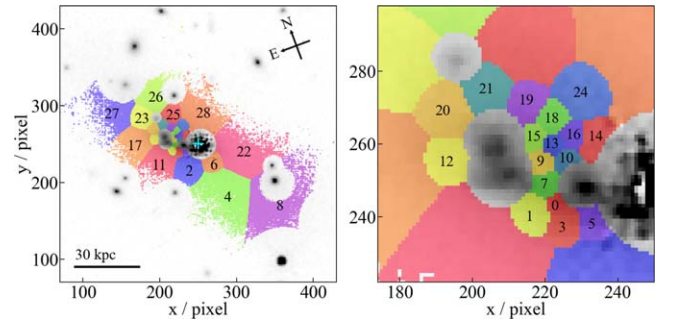


**Figure 4.** Left: segmentation map, where each tessellated region is color-coded differently, overlaid on the F160W image. IDs of each segment used in the main text are shown (also see Table 2). The position of 3C 186 is marked by a cyan cross symbol. Right: central region of the same Voronoi segmentation map. The region of the blue blob at  $[x, y] = [210, 260]$  (Section 3.3) is excluded from the host population analysis.

to the direction of the radio jet (Figure 3). We will discuss this in Section 4.1.

The choice of  $r_{\text{lim}}$  and the limiting S/N has only a minor effect on the estimate as long as  $S/N_{\text{limit}}$  is set to  $> 0.7$ ; having lower limiting S/N would significantly increase the estimated error due to noisy pixels across the entire image. On the other hand, the inferred offset becomes even larger when a higher value for  $S/N_{\text{limit}}$  is chosen. As in the middle panel of Figure 2, an ellipse fit to the F160W light profile shows a shift of the centroid in the northeast direction when only the central part of 3C 186 is used. This is due to the light concentration in the outskirts. We discuss the light concentration in relation to merger-induced morphological disturbances, or lack thereof, in Section 4.

Despite the depth that our new images reach, we might still be missing components with very low surface brightness ( $> 25$  mag arcsec $^{-2}$ ). However, we argue that such light components only marginally affect the determined photocenter. Our images here already reveal a substantial amount of stellar mass<sup>13</sup> ( $\log(M_*/M_\odot) \sim 11.4$ ; see Section 3.2). This amount is  $10\times$  more than what is found in the diffuse outskirts of low- $z$  elliptical galaxies (e.g., Huang et al. 2018).

### 3.2. Stellar Populations of the Host Galaxy

We aim to investigate the underlying stellar population in the host. The spatial distribution of stellar age enables us to estimate the timeline since the last merger and associated star formation activity.

To get sufficient S/N for reliable estimates out to faint outskirts of the host, we define subregions of the host by using a Voronoi tessellation method (Cappellari & Copin 2003). We set the minimum S/N to 15, so that every tessellated region has S/N greater than this value. As a result, at  $\sim 6''$  ( $\sim 48$  kpc) from the system LWC we reach down to  $\sim 25$  mag arcsec $^{-2}$  in F160W. We set the boundary of the host by using the segmentation mask generated by SExtractor with the detection threshold of 0.7, which is consistent with the threshold used for the LWC calculation above. Note that in this analysis, as it is not necessary for our purposes, we do not fill the masked regions defined in Section 3.1 and leave those empty. We show the defined mask and radial distribution of tessellated pixels in Figure 4.

<sup>13</sup> Such an amount of mass may be found in the diffuse stellar components but only in the most massive clusters (e.g., Morishita et al. 2017).



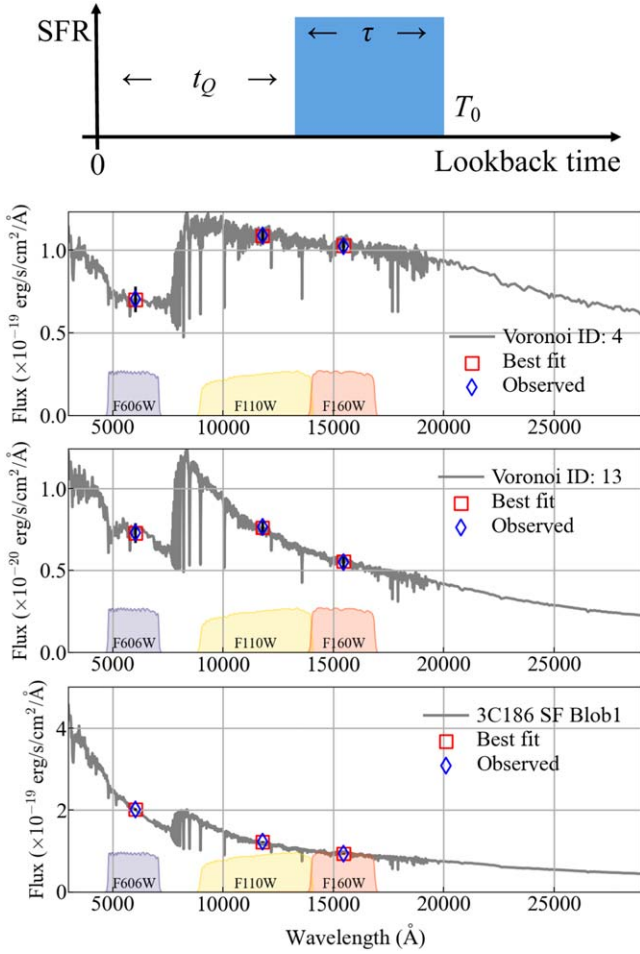


**Figure 5.** Top: schematic of our star formation history model, where star formation initiates at a time  $T_0$  ago, lasts continually for a time  $\tau$ , and then terminates a time  $t_Q$  ago. Bottom: examples of SED fitting results for three regions: Voronoi ID 4 (top), Voronoi ID 13 (middle), and SFB1 (bottom). The best-fit SEDs (solid lines) and convolved data points (red squares) are shown. Despite the small number of observed data points (three; blue diamonds), the data constrain the model by capturing the Balmer break ( $V_{606} - J_{110}$ ; sensitive to stellar age) and optical slope ( $J_{110} - H_{160}$ ; sensitive to dust). It is noted that at the redshift of 3C 186, F160W is free from strong emission lines such as  $H\alpha$ ,  $H\beta$ , and  $[O\ III]$ , making it a good tracer of the stellar component.

The boundary for tessellation defined in the F160W image is then applied to both F110W and F606W images, to collect flux from the same subregions. Each of the F110W and F606W images is convolved to the PSF size of the F160W image beforehand. The convolution kernels were generated by providing median-stacked PSFs to the Python software *pypher* (Boucaud et al. 2016), in the same way as in Morishita (2021). Fluxes of each subregion are summed and compiled into a catalog for a spectral energy distribution (SED) analysis in the following section.

The flux catalog collected from the tessellated images is provided to the SED fitting software *FAST* (Kriek et al. 2009). Due to the number of broadband filters available here (three), we are limited to a small number of fitting parameters. Since our primary focus here is to estimate the epoch of the last significant star formation (which could potentially be associated with major merger), we simply assume a single burst that started at  $T_0$  with a length of  $\tau$ . The schematic of this star formation model is shown in Figure 5.

We use the Bruzual & Charlot (2003) stellar population model, with the redshift fixed to the one estimated with the Sloan Digital Sky Survey DR6,  $z = 1.07$  (Hewett & Wild 2010), and the Calzetti et al. (2000) dust attenuation model. It is generally challenging to determine metallicity with only broadband photometry, and thus we fix it to solar. This is reasonable given that galaxies in this mass range are already metal-enriched, as seen at similar or earlier epochs (e.g., Thomas et al. 2010; Onodera et al. 2015; Kriek et al. 2019; Morishita et al. 2019).

In Figure 5, we show examples of the SED results in three different regions: the outer region ( $\sim 0''.9$  from the LWC; Voronoi ID 4), the inner ( $\sim 0''.2$  from the LWC; Voronoi ID 13), and the blue blob (see Section 3.3). These examples demonstrate that three data points are sufficient to constrain *relative* differences in age of different regions, by capturing both the Balmer break by  $V_{606} - J_{110}$  and the rest-frame optical slope by  $J_{110} - H_{160}$ . The best-fit parameters for all tessellated regions are summarized in Table 2.

A caveat is that with the number of data points used, degeneracy between age and dust is still not completely resolved, which makes inference of absolute values challenging. Our SED fitting results indicate small to moderate attenuation ( $A_V \lesssim 2.0$  mag). However, in the case of the 3C 186 host we do not expect significant dust attenuation, because no dust lane-like feature is seen in our HST images—such a feature would be clearly seen in the presence of significant dust attenuation (see, e.g., Skipper & Browne 2018; Hogg et al. 2021, for offset AGN candidates with clear dust lanes). In Figure 6, we show the two-dimensional distribution of  $J_{110} - H_{160}$  color of the host. While the color does not necessarily represent the exact dust attenuation due to the degeneracy, from the smooth morphology across the host it is unreasonable to expect significant dust structures.

In addition, Podigachoski et al. (2015) reported tentative detection ( $<3\sigma$ ) or nondetection of 3C 186 in far-IR bands, at 160, 250, 350, and 500  $\mu\text{m}$  by the Herschel Space Observatory, implying no significant amount of dust is present in the system. Fixing dust attenuation to zero would increase the age estimates, to account for red components; therefore, our age estimates, especially those with nonzero  $A_V$ , should be taken as lower limits.

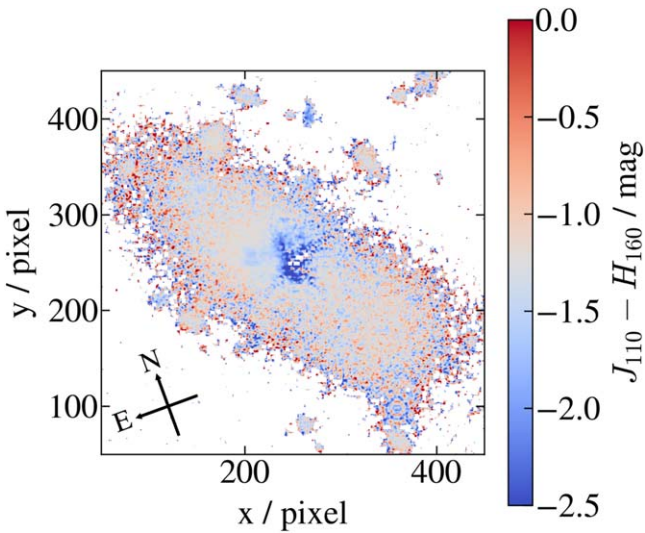
In Figure 7, we show the spatial distribution of each of the derived parameters. Our interest here is in  $T_0$ , the time at which primary star formation started, and  $t_Q$ , which we introduce to refer to length of time since star formation was truncated ( $\equiv T_0 - \tau$ ). There is no clear radial trend for  $T_0$ , with a median value of  $160^{+200}_{-40}$  Myr, with the associated errors capturing the 16th/84th percentiles. Similarly, no clear spatial correlation nor radial trend is observed for  $t_Q$ . The parameter ranges from  $\sim 30$  to  $\sim 500$  Myr, with a median value of  $t_Q = 90^{+110}_{-30}$  Myr, except in a few subregions with ongoing star formation (i.e.,  $t_Q \leq 0$ ). The total mass, derived by summing the best-fit estimate over the Voronoi segments, is found to be  $\log(M_*/M_\odot) = 11.4$ .

### 3.3. Compact Blue Star-forming Region in the Host Galaxy

As we highlight in the color-composite image of Figure 1, there is a compact star-forming blob (SFB1 hereafter) located at  $\sim 2''$  from the quasar in the northeast direction. This blob was seen in the early data and reported in Chiaberge et al. (2017), but its properties remained unclear. Our SED modeling revealed its age,  $T_0 \sim 160$  Myr, and stellar mass,  $\sim 8 \times 10^9 M_\odot$  (Figure 5).

**Table 2**  
Positions of Tessellated Segments and the Best-fit SED Parameters

Voronoi ID	S/N	$r^a$ (arcsec)	$\log(M_*/M_\odot)$	$\log(T_0/\text{yr})$	$\log(\tau/\text{yr})$	$\log(t_Q/\text{yr})$	$A_V$ (mag)
0	19.0	0.59	9.2	8.1	7.8	7.8	1.7
1	22.8	0.80	9.6	8.1	7.0	8.1	1.5
2	26.7	1.91	10.0	8.0	7.2	7.9	1.2
3	23.1	0.86	9.6	8.5	7.8	8.4	1.2
4	23.9	4.40	10.7	9.4	9.8	... <sup>b</sup>	1.3
5	21.0	0.92	9.4	8.8	8.2	8.7	0.0
6	23.1	2.51	9.9	8.3	7.0	8.3	1.1
7	23.4	0.35	9.2	8.0	7.6	7.8	1.3
8	22.3	7.06	10.6	8.3	7.6	8.2	2.1
9	18.7	0.20	9.0	7.9	7.0	7.8	1.0
10	19.3	0.12	9.2	8.3	7.6	8.2	0.9
11	22.5	1.84	10.0	8.1	8.0	7.4	1.7
12	23.4	1.36	9.7	8.8	9.4	... <sup>b</sup>	1.6
13	15.7	0.18	8.9	8.0	7.0	8.0	0.9
14	20.3	0.55	9.3	8.6	8.2	8.4	0.0
15	18.2	0.39	9.0	7.9	7.2	7.8	1.0
16	16.4	0.36	9.1	8.5	8.0	8.3	0.4
17	22.1	2.60	10.3	8.1	7.6	7.9	2.1
18	17.9	0.49	9.2	8.0	7.0	8.0	1.2
19	21.5	0.81	9.5	7.9	7.0	7.8	1.6
20	26.0	1.52	9.7	8.0	7.8	7.6	1.8
21	20.8	1.21	9.6	7.9	7.4	7.7	1.8
22	26.1	3.87	10.4	8.1	7.6	7.9	1.6
23	22.3	2.51	10.2	8.3	7.8	8.1	1.9
24	22.4	0.86	9.5	8.5	7.0	8.5	0.0
25	23.8	1.52	9.8	8.4	9.6	... <sup>b</sup>	1.7
26	18.1	2.86	10.1	8.7	10.0	... <sup>b</sup>	1.8
27	15.4	4.21	10.3	8.2	7.6	8.1	2.2
28	24.9	2.12	10.1	8.3	8.0	8.0	0.6

**Notes.**<sup>a</sup> Distance from the light-weighted center.<sup>b</sup> Regions with ongoing star formation (i.e.,  $t_Q = 0$ ).

**Figure 6.** Two-dimensional  $J_{110} - H_{160}$  color map of the host of 3C 186. Note that the quasar component is subtracted from each of the images used here. The image exhibits smooth morphology across the host, except for two blue regions near the quasar (mostly residual) and the blue blob (Section 3.3). The outer regions of the host are excluded and set to blank.

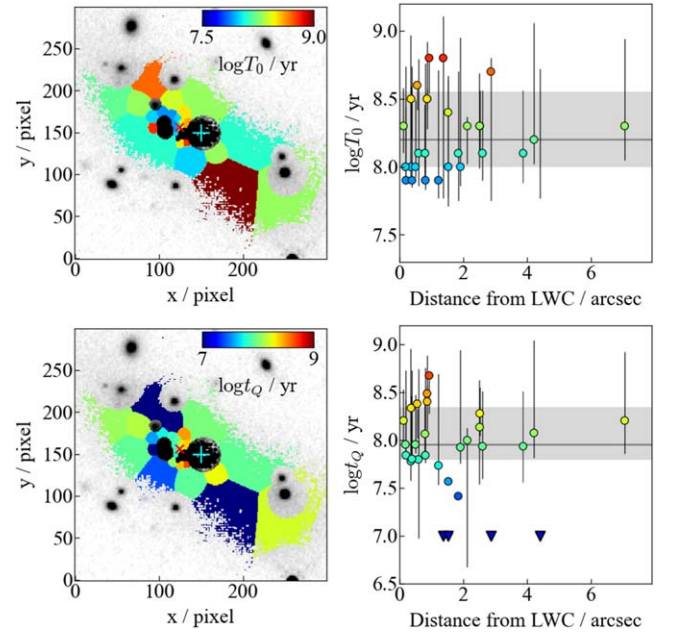


**Figure 7.** Spatial and radial distributions of two parameters,  $T_0$  (top row) and  $t_Q$  (bottom), are shown. Colors in the radial distribution plots correspond to those in the spatial distribution plots. Four of the tessellated pixels show ongoing star formation (i.e.,  $t_Q = 0$ ) and are shown at an arbitrary value (blue triangle).

We estimate its star formation rate (SFR),  $65 \pm 20 M_{\odot} \text{ yr}^{-1}$ , by averaging over the last 100 Myr of the best-fit star formation history, which is consistent with the upper limit of the whole system derived from nondetection in Herschel data,  $<80 M_{\odot} \text{ yr}^{-1}$  (Podigachoski et al. 2015).

The best-fit SFR converts to a star formation rate surface density of  $\sim 1.2 M_{\odot} \text{ yr}^{-1} \text{ kpc}^{-2}$ . Considering its stellar surface density ( $\log \Sigma_{*} \sim 8.1 M_{\odot} \text{ kpc}^{-2}$ ), this value is  $\sim 0.8$  dex higher than the average value of resolved subregions in star-forming galaxies at  $z \sim 1$  (e.g., Wuyts et al. 2013), indicating intense star formation activity may still be ongoing in the host despite relatively old stellar populations elsewhere. Such intense star formation is actually seen in a post-merger system (e.g., Barrows et al. 2018) but lasts only for a short timescale of  $\sim 100$  Myr. We revisit this in Section 4.

Since the template library used in the SED fitting in Section 3.2 does not include emission lines, we check the fidelity by running another SED fitting code, *gsf* (Morishita et al. 2019), with emission lines included. While an exponentially declining star formation history is used this time, due to the limitation of the code, it derives a consistent value for star formation rate,  $70 \pm 10 M_{\odot} \text{ yr}^{-1}$ .

While the IFU observations presented in Chiaberge et al. (2018) covered SFB1, no line was detected, because the observations were originally designed for the brightness of the quasar and exposure was not deep enough to detect any emission lines in SFB1. Recent observations at NOEMA detected extended CO emission near the flux peak position of SFB1 at the same redshift as the optical narrow lines (Castignani et al. 2022).

## 4. Discussion

### 4.1. On the Dynamics of the GW Recoil

As we introduced in Section 1, based on its spectroscopic and imaging properties, 3C 186 was proposed as a clear example of a GW recoiling black hole candidate by Chiaberge et al. (2017). With our deep HST observations, we both confirmed and more accurately determined the presence of a spatial offset between the quasar and the host photocenter. Based on our results (Section 3.1), we see that the direction of the putative GW kick lies perpendicular to the radio jet axis. In Figure 3, we show the 8.44 GHz radio continuum emission overlaid on the central region of the host galaxy. The direction of the kick is at the position angle of  $\sim +33^{\circ}$ , while the radio jet axis has a position angle of  $\sim -57^{\circ}$ . As pointed out by, e.g., Lousto et al. (2012), the maximum velocity of a GW kick ( $>2000 \text{ km s}^{-1}$ ) may be more likely achieved if the direction of the kick is aligned with the angular momentum of the orbital plane of the merging black hole binary. Since the radio jet axis likely indicates the orientation of the spin of the merged black hole, these results may impose further constraints on the properties of the progenitor binary, in particular with respect to the spin amplitude and relative orientation. A detailed modeling of the binary black hole system and the GW recoil kick lies beyond the scope of this work.

### 4.2. Insight Into the Current Evolutionary Stage

In this subsection, we discuss the main results of this work, which focuses on the observed properties of the host. This allows us to speculate on the current evolutionary stage of this system. Chiaberge et al. (2017) reported a possible shell or tidal

feature in the host light profile and suggested its origin as a major merger that occurred about  $\sim 1$  Gyr ago from comparison with numerical simulations. Our F160W image presented here revealed even fainter stellar components out to  $\sim 60$  kpc from the LWC of the host. While a slight light concentration is seen in the outermost part in the southeast direction, we did not see clear evidence of disturbed morphology or young star clusters in its outskirts, which would be characteristic of ongoing merger (e.g., Mulia et al. 2015), implying that the system is a relatively old, post-merger remnant. Furthermore, Podigachoski et al. (2015) derived high SFR in other 3C galaxies at similar redshifts, most of which are associated with ongoing mergers, whereas an upper limit was estimated for 3C186 from nondetection in their Herschel data ( $<80 M_{\odot} \text{ yr}^{-1}$ ). This suggests that 3C 186 is older than other 3C systems in terms of recent star formation too.

To further investigate the current evolutionary phase of 3C 186, we compare the observed properties with hydrodynamical simulations. In Figure 8, we show a time sequence of a merging system from the VELA-Sunrise project (Simons et al. 2019). The VELA-Sunrise project provides a set of mock images of simulated galaxies that were originally taken from the VELA simulation suite (Ceverino et al. 2014; Zolotov et al. 2015). The simulation suite consists of a variety of galaxies at different evolutionary stages, including both isolated and merging systems. While the original simulations do not include specific recipes for black hole mergers, the data sets offer detailed morphological information of, e.g., a galaxy during merger sequences, at the resolution of HST. Here we select VELA04, one of the merging systems available in the VELA suite. Specifically, the data set of VELA04 captures the timeline of pre- to post-merger and allows us to investigate the evolutionary stage of 3C 186 by comparing their morphological properties.

The example shown in Figure 8 is a sequence that captures the pre-merger to post-merger phases of two galaxies at  $z \sim 2$ . The sequence exhibits several features that resemble the observed properties of the 3C 186 host. The last frame of Figure 8 captures the elongated (but not disturbed) morphology of the host galaxy and compact star-forming regions in the main body of the host. We also see the presence of young, compact blue regions across the entire sequence. Those blue regions do not appear in more than one simulation frame, implying that their lifetime is less than its time resolution,  $\lesssim 200$  Myr. In the last frame of the sequence in Figure 8, we highlight one such compact blue region. Its specific star formation rate is  $\sim 40 \text{ Gyr}^{-1}$  (cf.  $\sim 8 \text{ Gyr}^{-1}$  of the blue blob in 3C 186). The rest of the stellar populations of the galaxy in the frame are relatively old, with a median age of  $\sim 1$  Gyr (cf.  $\gtrsim 200$  Myr in 3C 186). While we also notice morphological differences between the two systems (e.g., more clumps and less relaxed), those physical properties are broadly consistent with the observed properties of 3C 186 (Section 3.3).

The spatial offset found in this study is encouraging regarding a typical timescale after a recoiling event. By using the derived spatial offset of the quasar from the LWC (Section 3.1) and the velocity offset derived in Chiaberge et al. (2017), we estimate that the recoil event occurred  $\gtrsim 5$  Myr ago, though the exact age depends on the assumed kick angle. Theoretically, it is possible for a recoiling black hole to remain active for such a length of time. By using the formula in Loeb (2007) with assumed radiative efficiency of  $\epsilon = 0.1$  as in



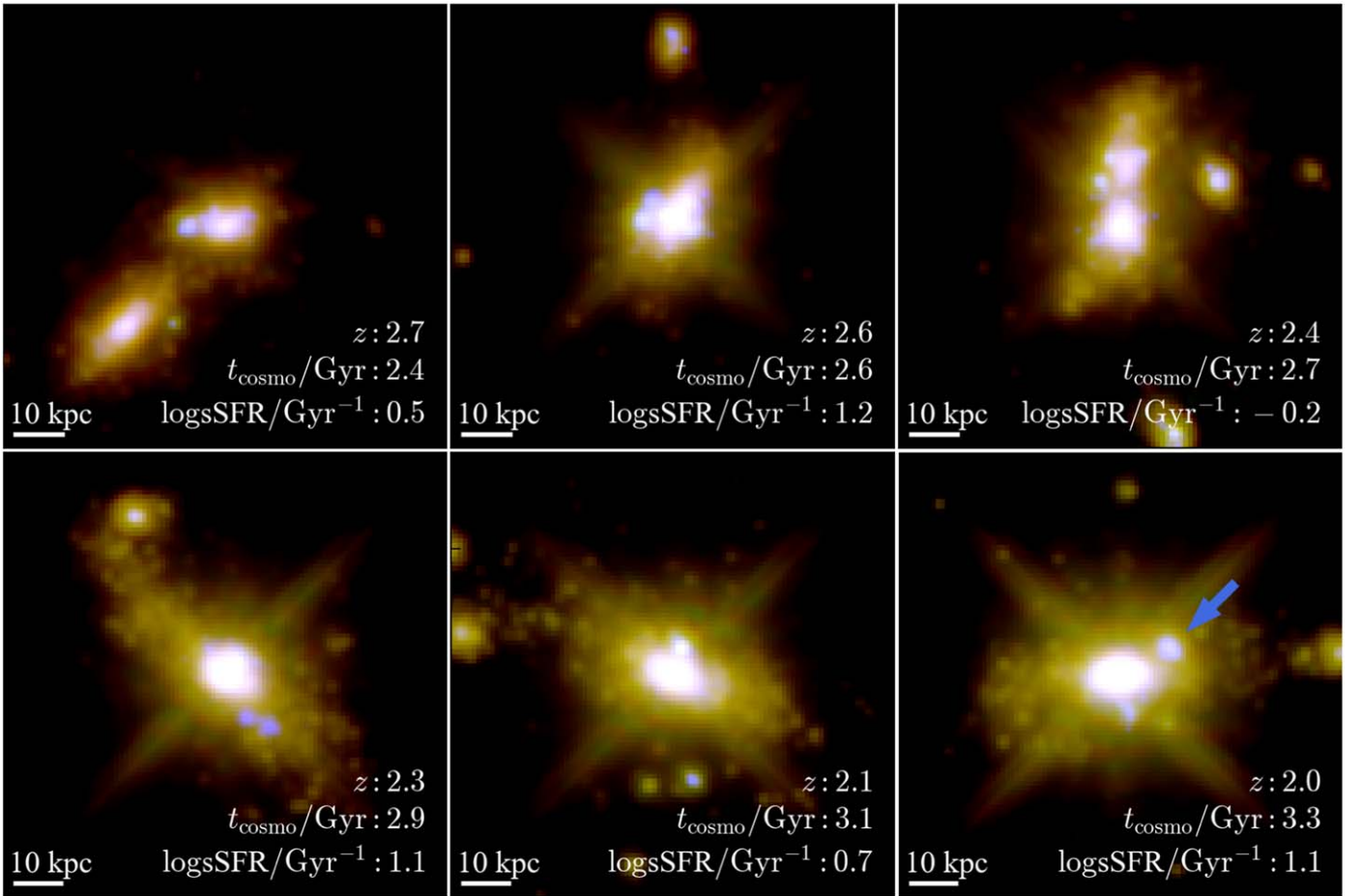


**Figure 8.** A sequence of the merging system VELA04 (Camera05) at  $2.0 < z < 2.7$ , taken from the VELA-Sunrise simulation suite. Redshift, cosmic time, and specific star formation rate of each frame are shown. The RGB composite images consist of F814W, F125W, and F160W, to compensate for its higher redshift than 3C 186’s. One of the star-forming regions (see Section 4) is indicated by a blue arrow in the last frame.

Chiaberge et al. (2017), the lifetime of an accretion disk for the black hole mass of 3C 186 is estimated to be  $\sim 100$  Myr. In fact, Murgia et al. (1999) derived the age of the radio source in 3C 186,  $\sim 0.1$  Myr, from its synchrotron spectrum, which implies that the radio AGN turned on after the recoiling event.

In addition, Blecha et al. (2011) presented several examples of simulated recoiling black holes and estimated a typical lifetime of  $\sim 10$  Myr (see also Blecha et al. 2016). We note, however, that uncertainties in absolute timescale in those simulations are not negligible. Such uncertainties primarily originate in the resolution element, which is typically much larger than the scale of black hole merger (several kiloparsecs), making the comparison with observations challenging. This is still the case with more recent simulations that record the exact time of the black hole merger (e.g., TNG; Hani et al. 2020). Sub-grid models of black hole binary evolution (e.g., Kelley et al. 2017) show a wide range of black hole merger timescales, from  $\sim 1$  Gyr to more than a Hubble time, depending on the model assumptions and the specific conditions in the galactic nuclei.

#### 4.3. Alternative Scenario

As we mentioned in Section 1, there is an alternative scenario for the observed spatial offset, where the quasar is hosted by another, fainter galaxy (“galaxy B” for convenience) that is superposed on a galaxy at different redshift (“galaxy A”

i.e., the one we have analyzed in this study as the host). However, this scenario is unlikely because (1) we did not confirm any stellar light concentration near the position of the quasar in any filters and (2) there is evidence of narrow absorption at the same redshift as the narrow emission lines.

For (1), assuming the scaling relation between  $M_*$  and  $M_{\text{BH}}$  (e.g., Kormendy & Ho 2013), stellar mass  $M_* \sim 10^{12} M_\odot$  is expected for the black hole mass of 3C 186,  $M_{\text{BH}} \sim (3-6) \times 10^9 M_\odot$ . Such a mass should be noticeable in our F160W image regardless of its light profile. Chiaberge et al. (2017) tested this with various structural parameters for unseen galaxy B by using *galfit* (Peng et al. 2002) but concluded that one is not likely not to see such a mass even in their F140W image. The recoiling black hole scenario, which assumes galaxy A ( $\log(M_*/M_\odot) \sim 11.4$ ; Section 3.2) as the host, offers more reasonable agreement in terms of the scaling relation for the stellar and black hole masses observed. To further investigate this scenario, we repeat the structural analyses by using our deep F160W image. We provide the original image with the quasar component unsubtracted as the input image to *galfit*. We fit the light profile of the 3C 186 system with one PSF component at the position of the quasar, one Sérsic component fixed at the LWC position derived above, and one additional Sérsic component (i.e., galaxy B) at the quasar position. We fix the position angle and axis ratio of the host to  $36^\circ$  and 0.37 (Chiaberge et al. 2017), respectively, and leave all other

parameters free. We find that the second Sérsic component does not improve the fit. The best-fit effective radius of this additional component is unphysically small, 54 mas. In addition, the total flux of this component remains at  $\sim 7\%$  of the host. This converts to a stellar mass of  $\sim 1.8 \times 10^{10} M_{\odot}$  by adopting the same mass-to-light ratio as the host, which is significantly undermassive for the black hole mass of 3C 186. We therefore conclude that this additional component, if not an artifact such as flux residuals of the PSF component, is unlikely to be the unseen host galaxy of the quasar.

For (2), Chiaberge et al. (2017) found narrow absorption features in both Ly $\alpha$  and [C IV] lines at the same redshift as the narrow emission lines ([O II] and [Ne III]). This indicates the presence of gas associated with galaxy A and thus secures its redshift (see also Castignani et al. 2022, who identified CO emission at the same redshift as the narrow lines within the host). Determining the systemic redshift of galaxy A directly from stellar absorption lines will be a critical step to test the scenario.

#### 4.4. Future Prospects

Lastly, we note that the observed blueshift measured in the permitted broad lines should carefully be interpreted, because these have large uncertainties primarily due to broad absorption components and blending with other lines (Chiaberge et al. 2017). For example, such broad absorption is often associated with extreme outflow and seen in a number of local AGNs (Kaastra et al. 2014; Ebrero et al. 2016), making it challenging to attribute the observed blueshift solely to a recoiling event. An ideal line is H $\beta$ , which is a good tracer of the kinematics of the accretion disk/inner broad-line region *and* is isolated from other emission lines; thus it can provide a clean measurement of the velocity shift of the accretion disk (Chiaberge et al. 2018). However, this line is located at  $\sim 1 \mu\text{m}$  for the redshift (plus possible large blueshift) of 3C 186, and access to the entire line profile with current spectrographs may be challenging due to atmospheric absorption and the gap between CCD and IR detector. The IFU mode of NIRSpec on the James Webb Space Telescope (JWST) would be an ideal choice, allowing us to confirm the velocity shift and to locate spatial distribution simultaneously.

High-resolution submillimeter/millimeter observations of dense gas in 3C 186 would also be a critical step to confirm the physical origin of the blueshift. This is because dense gas in the molecular torus is considered to be orbiting at large distances and thus not gravitationally bounded to the recoiling black hole itself. Indeed, Decarli et al. (2014) tested this on a candidate, QSO J0927+2943 at  $z=0.697$ , and identified molecular gas traced by the CO(2–1) line at the redshift of the quasar’s broad line, arguing the need for another scenario to explain the properties of the quasar (see also Heckman et al. 2009; Shields et al. 2009).

## 5. Summary

In this study, we investigated the properties of the host of 3C 186, a recoiling black hole candidate at  $z=1.0685$ . By carefully analyzing newly taken deep images from HST, we confirmed the previously reported spatial offset,  $11.1 \pm 0.1$  kpc in projected distance, between the core of 3C 186 and the light-weighted center of the host galaxy. We did not find evidence of a recent merger, such as a young starburst in disturbed











outskirts. We analyzed the underlying stellar populations of the host and then compared the observed properties with numerical simulations, finding that the observed properties of 3C 186 are consistent with an old merger remnant. Based on those pieces of evidence, we concluded that the recoiling black hole scenario is still a plausible explanation for the puzzling nature of 3C 186.

Lastly, we wish to stress that 3C 186 has one of the highest redshifts for a candidate recoiling black hole that has been identified as of today. Given the higher merger rate at high redshift (e.g., Lotz et al. 2011; Snyder et al. 2017), it is reasonable to expect that more candidates will be identified in systematic high-resolution imaging surveys of radio quasars at similar redshifts. Future observations with high-resolution imaging cameras of JWST, even with the short exposure time available in, e.g., Survey programs,<sup>14</sup> will allow us to identify more recoiling black hole candidates and investigate the ubiquity of this extreme phenomenon.

We thank the anonymous referee for the constructive comments. We thank Emanuele Berti and Davide Gerosa for fruitful discussion on the physical interpretation of our findings, and Markos Georganopoulos, Andrea Marinucci, Eileen Meyer, Eric S. Perlman, William B. Sparks, and Grant R. Tremblay for their contribution to the HST observing program GO-15254. M.C. thanks Marta Volonteri for providing constructive comments on our study. Support for this study was provided by NASA through a grant HST-GO-15254.005-A from the Space Telescope Science Institute, which is operated by the Association of Universities for Research in Astronomy, Inc., under NASA contract NAS 5-26555. This work is based in part on observations taken by the VLA, operated by the U.S. National Radio Astronomy Observatory, which is a facility of the National Science Foundation, operated under cooperative agreement by Associated Universities, Inc. L.B. acknowledges support from NSF award AST-1909933. S.B. and C.O. acknowledge support from the Natural Sciences and Engineering Research Council (NSERC) of Canada. G.C. acknowledges the support from the grant ASI n.2018-23-HH.0.

*Software:* Astropy (Astropy Collaboration et al. 2013, 2018), Astrodizzle (Hack et al. 2012), FAST (Kriek et al. 2009), GALFIT (Peng et al. 2002, 2010), gsf (Morishita et al. 2019), LACOSMIC (van Dokkum et al. 2001), numpy (Oliphant 2006; Van Der Walt et al. 2011), Pypher (Boucaud et al. 2016), SExtractor (Bertin & Arnouts 1996).

## ORCID iDs

T. Morishita  <https://orcid.org/0000-0002-8512-1404>  
M. Chiaberge  <https://orcid.org/0000-0003-1564-3802>  
B. Hilbert  <https://orcid.org/0000-0002-6875-1543>  
E. Lambrides  <https://orcid.org/0000-0003-3216-7190>  
L. Blecha  <https://orcid.org/0000-0002-2183-1087>  
S. Bianchi  <https://orcid.org/0000-0002-4622-4240>  
A. Capetti  <https://orcid.org/0000-0003-3684-4275>  
G. Castignani  <https://orcid.org/0000-0001-6831-0687>  
C. P. O’Dea  <https://orcid.org/0000-0001-6421-054X>  
C. A. Norman  <https://orcid.org/0000-0002-5222-5717>

<sup>14</sup> <https://jwst-docs.stsci.edu/jwst-opportunities-and-policies/jwst-call-for-proposals-for-cycle-1/jwst-cycle-1-proposal-categories/general-observer-go-proposals/survey-go-proposals>

## References

- Anderson, J., & Bedin, L. R. 2010, *PASP*, **122**, 1035
- Astropy Collaboration, Price-Whelan, A. M., Sipőcz, B. M., et al. 2018, *AJ*, **156**, 123
- Astropy Collaboration, Robitaille, T. P., Tollerud, E. J., et al. 2013, *A&A*, **558**, A33
- Barrows, R. S., Comerford, J. M., & Greene, J. E. 2018, *ApJ*, **869**, 154
- Barrows, R. S., Comerford, J. M., Greene, J. E., & Pooley, D. 2016, *ApJ*, **829**, 37
- Batcheldor, D., Robinson, A., Axon, D. J., Perlman, E. S., & Merritt, D. 2010, *ApJL*, **717**, L6
- Begelman, M. C., Blandford, R. D., & Rees, M. J. 1980, *Natur*, **287**, 307
- Bertin, E., & Arnouts, S. 1996, *A&AS*, **117**, 393
- Blecha, L., Civano, F., Elvis, M., & Loeb, A. 2013, *MNRAS*, **428**, 1341
- Blecha, L., Cox, T. J., Loeb, A., & Hernquist, L. 2011, *MNRAS*, **412**, 2154
- Blecha, L., Sijacki, D., Kelley, L. Z., et al. 2016, *MNRAS*, **456**, 961
- Boucaud, A., Bocchio, M., Abergel, A., et al. 2016, *A&A*, **596**, A63
- Bruzual, G., & Charlot, S. 2003, *MNRAS*, **344**, 1000
- Burke-Spolaor, S., Gültekin, K., Postman, M., et al. 2017, *ApJ*, **849**, 59
- Calzetti, D., Amus, L., Bohlin, R. C., et al. 2000, *ApJ*, **533**, 682
- Campanelli, M., Lousto, C. O., Zlochower, Y., & Merritt, D. 2007, *PhRvL*, **98**, 231102
- Cappellari, M., & Copin, Y. 2003, *MNRAS*, **342**, 345
- Castignani, G., Meyer, E., Chiaberge, M., et al. 2022, *A&A*, **661**, L2
- Centrella, J., Baker, J. G., Kelly, B. J., & van Meter, J. R. 2010, *RvMP*, **82**, 3069
- Ceverino, D., Klypin, A., Klimek, E. S., et al. 2014, *MNRAS*, **442**, 1545
- Chiaberge, M., Ely, J. C., Meyer, E. T., et al. 2017, *A&A*, **600**, A57
- Chiaberge, M., Tremblay, G. R., Capetti, A., & Norman, C. 2018, *ApJ*, **861**, 56
- Civano, F., Elvis, M., Lanzuisi, G., et al. 2010, *ApJ*, **717**, 209
- Civano, F., Elvis, M., Lanzuisi, G., et al. 2012, *ApJ*, **752**, 49
- Comerford, J. M., & Greene, J. E. 2014, *ApJ*, **789**, 112
- Decarli, R., Dotti, M., Mazzucchelli, C., Montuori, C., & Volonteri, M. 2014, *MNRAS*, **445**, 1558
- Dotti, M., Colpi, M., Haardt, F., & Mayer, L. 2007, *MNRAS*, **379**, 956
- Ebrero, J., Kriss, G. A., Kaastra, J. S., & Ely, J. C. 2016, *A&A*, **586**, A72
- Escala, A., Larson, R. B., Coppi, P. S., & Mardones, D. 2005, *ApJ*, **630**, 152
- Fanti, C., Fanti, R., Parma, P., Schilizzi, R. T., & van Breugel, W. J. M. 1985, *A&A*, **143**, 292
- Ferrarese, L., & Merritt, D. 2000, *ApJL*, **539**, L9
- Frank, J., & Rees, M. J. 1976, *MNRAS*, **176**, 633
- Fukugita, M., Ichikawa, T., Gunn, J. E., et al. 1996, *AJ*, **111**, 1748
- Gebhardt, K., Richstone, D., Kormendy, J., et al. 2000, *AJ*, **119**, 1157
- Glikman, E., Djorgovski, S. G., Stern, D., Bogosavljević, M., & Mahabal, A. 2007, *ApJL*, **663**, L73
- Goulding, A. D., Pardo, K., Greene, J. E., et al. 2019, *ApJL*, **879**, L21
- Hack, W. J., Dencheva, N., Fruchter, A. S., et al. 2012, AAS Meeting Abstracts, **220**, 135.15
- Hani, M. H., Gosain, H., Ellison, S. L., Patton, D. R., & Torrey, P. 2020, *MNRAS*, **493**, 3716
- Heckman, T. M., Krolak, J. H., Moran, S. M., Schnittman, J., & Gezari, S. 2009, *ApJ*, **695**, 363
- Hennawi, J. F., Strauss, M. A., Oguri, M., et al. 2006, *AJ*, **131**, 1
- Hewett, P. C., & Wild, V. 2010, *MNRAS*, **405**, 2302
- Hilbert, B., Chiaberge, M., Kotyla, J. P., et al. 2016, *ApJS*, **225**, 12
- Hogg, J. D., Blecha, L., Reynolds, C. S., Smith, K. L., & Winter, L. M. 2021, *MNRAS*, **503**, 1688
- Huang, S., Leauthaud, A., Greene, J. E., et al. 2018, *MNRAS*, **475**, 3348
- Kaastra, J. S., Kriss, G. A., Cappi, M., et al. 2014, *Sci*, **345**, 64
- Kelley, L. Z., Blecha, L., & Hernquist, L. 2017, *MNRAS*, **464**, 3131
- Kim, D. C., Yoon, I., Privon, G. C., et al. 2017, *ApJ*, **840**, 71
- Komossa, S. 2012, *AdAst*, **2012**, 364973
- Komossa, S., Burwitz, V., Hasinger, G., et al. 2003, *ApJL*, **582**, L15
- Komossa, S., Zhou, H., & Lu, H. 2008, *ApJL*, **678**, L81
- Kormendy, J., & Ho, L. C. 2013, *ARA&A*, **51**, 511
- Koss, M., Blecha, L., Mushotzky, R., et al. 2014, *MNRAS*, **445**, 515
- Koss, M. J., Blecha, L., Bernhard, P., et al. 2018, *Natur*, **563**, 214
- Kriek, M., Price, S. H., Conroy, C., et al. 2019, *ApJL*, **880**, L31
- Kriek, M., van Dokkum, P. G., Labbé, I., et al. 2009, *ApJ*, **700**, 221
- Krist, J. E., Hook, R. N., & Stoehr, F. 2011, *Proc. SPIE*, **8127**, 81270J
- Kuraszkiewicz, J. K., Green, P. J., Forster, K., et al. 2002, *ApJS*, **143**, 257
- Lena, D., Robinson, A., Marconi, A., et al. 2014, *ApJ*, **795**, 146
- Loeb, A. 2007, *PhRvL*, **99**, 041103
- Lotz, J. M., Jonsson, P., Cox, T. J., et al. 2011, *ApJ*, **742**, 103
- Lousto, C. O., & Zlochower, Y. 2011, *PhRvL*, **107**, 231102
- Lousto, C. O., Zlochower, Y., & Campanelli, M. 2017, *ApJL*, **841**, L28
- Lousto, C. O., Zlochower, Y., Dotti, M., & Volonteri, M. 2012, *PhRvD*, **85**, 084015
- Milosavljević, M., & Merritt, D. 2003, *ApJ*, **596**, 860
- Moore, C. J., Cole, R. H., & Berry, C. P. L. 2015, *CQGra*, **32**, 015014
- Morishita, T. 2021, *ApJS*, **253**, 4
- Morishita, T., Abramson, L. E., Treu, T., et al. 2017, *ApJ*, **835**, 254
- Morishita, T., Abramson, L. E., Treu, T., et al. 2019, *ApJ*, **877**, 141
- Mulia, A. J., Chandar, R., & Whitmore, B. C. 2015, *ApJ*, **805**, 99
- Murgia, M., Fanti, C., Fanti, R., et al. 1999, *A&A*, **345**, 769
- Novak, M., Smolčić, V., Civano, F., et al. 2015, *MNRAS*, **447**, 1282
- O'Dea, C. P. 1998, *PASP*, **110**, 493
- O'Dea, C. P., & Saikia, D. J. 2021, *A&ARv*, **29**, 3
- Oke, J. B., & Gunn, J. E. 1983, *ApJ*, **266**, 713
- Oliphant, T. E. 2006, A Guide to NumPy, Vol. 1 (USA: Trelgol Publishing)
- O'Neill, S., Kiehlmann, S., Readhead, A. C. S., et al. 2022, *ApJL*, **926**, L35
- Onodera, M., Carollo, C. M., Renzini, A., et al. 2015, *ApJ*, **808**, 161
- Peng, C. Y. 2007, *ApJ*, **671**, 1098
- Peng, C. Y., Ho, L. C., Impey, C. D., & Rix, H.-W. 2002, *AJ*, **124**, 266
- Peng, Y.-j., Lilly, S. J., Kovač, K., et al. 2010, *AJ*, **139**, 2097
- Pesce, D. W., Braatz, J. A., Condon, J. J., & Greene, J. E. 2018, *ApJ*, **863**, 149
- Pesce, D. W., Seth, A. C., Greene, J. E., et al. 2021, *ApJ*, **909**, 141
- Podigachoski, P., Barthel, P. D., Haas, M., et al. 2015, *A&A*, **575**, A80
- Postman, M., Lauer, T. R., Donahue, M., et al. 2012, *ApJ*, **756**, 159
- Salpeter, E. E. 1955, *ApJ*, **121**, 161
- Shields, G. A., Rosario, D. J., Smith, K. L., et al. 2009, *ApJ*, **707**, 936
- Siemiginowska, A., Cheung, C. C., LaMassa, S., et al. 2005, *ApJ*, **632**, 110
- Silverman, J. D., Tang, S., Lee, K.-G., et al. 2020, *ApJ*, **899**, 154
- Simons, R. C., Kassin, S. A., Snyder, G. F., et al. 2019, *ApJ*, **874**, 59
- Skipper, C. J., & Browne, I. W. A. 2018, *MNRAS*, **475**, 5179
- Snyder, G. F., Lotz, J. M., Rodríguez-Gomez, V., et al. 2017, *MNRAS*, **468**, 207
- Springel, V. 2005, *MNRAS*, **364**, 1105
- Steinhardt, C. L., Schramm, M., Silverman, J. D., et al. 2012, *ApJ*, **759**, 24
- Thomas, D., Maraston, C., Schawinski, K., Sarzi, M., & Silk, J. 2010, *MNRAS*, **404**, 1775
- Tichy, W., & Marronetti, P. 2007, *PhRvD*, **76**, 061502
- Van Der Walt, S., Colbert, S. C., & Varoquaux, G. 2011, *CSE*, **13**, 22
- van Dokkum, P. G., Franx, M., Kelson, D. D., & Illingworth, G. D. 2001, *ApJL*, **553**, L39
- Volonteri, M., Haardt, F., & Madau, P. 2003, *ApJ*, **582**, 559
- Wuyts, S., Förster Schreiber, N. M., Nelson, E. J., et al. 2013, *ApJ*, **779**, 135
- Zolotov, A., Dekel, A., Mandelker, N., et al. 2015, *MNRAS*, **450**, 2327